




 Cite this: *RSC Adv.*, 2023, **13**, 14041

An electrothermal platform for active droplet manipulation†

 Yahua Liu, ^{ab} Yuhang Xia,^a Haiyang Zhan,^a Chenguang Lu,^a Zichao Yuan^a and Lei Zhao ^{*a}

The smart control of droplet transport through surface structures and external fields provides exciting opportunities in engineering fields of phase change heat transfer, biomedical chips, and energy harvesting. Here we report the wedge-shaped slippery lubricant-infused porous surface (WS-SLIPS) as an electrothermal platform for active droplet manipulation. WS-SLIPS is fabricated by infusing a wedge-shaped superhydrophobic aluminum plate with phase-changeable paraffin. While the surface wettability of WS-SLIPS can be readily and reversibly switched by the freezing–melting cycle of paraffin, the curvature gradient of the wedge-shaped substrate automatically induces an uneven Laplace pressure inside the droplet, endowing WS-SLIPS the ability to directionally transport droplets without any extra energy input. We demonstrate that WS-SLIPS features spontaneous and controllable droplet transport capability to initiate, brake, lock, and resume the directional motion of various liquid droplets including water, saturated NaCl solution, ethanol solution, and glycerol, under the control of preset DC voltage (~12 V). In addition, the WS-SLIPS can automatically repair surface scratches or indents when heated and retain the full liquid-manipulating capability afterward. The versatile and robust droplet manipulation platform of WS-SLIPS can be further used in practical scenarios such as laboratory-on-a-chip settings, chemical analysis and microfluidic reactors, paving a new path to develop advanced interface for multifunctional droplet transport.

Received 18th February 2023

Accepted 24th April 2023

DOI: 10.1039/d3ra01108a

rsc.li/rsc-advances

1. Introduction

On-demand manipulation of microvolume droplets on surfaces has attracted remarkable attention due to its crucial importance in the fields of microfluidic reactors,^{1,2} bioassay,^{3–5} and molecular sensing.^{6–8} To serve this purpose, static approaches that integrates asymmetric surface textures have been devised to passively alter the dimension, direction, and velocity of droplet transport on designated functional surfaces.^{9–14} Furthermore, surfaces incorporating stimulus-responsive elements that respond to electrical,^{15–18} magnetic,^{19–21} thermal^{22–24} and acoustic^{25–27} stimuli are endowed with intelligent functionalities to manipulate the mobility of residing droplets by reversible structural restructuring and chemical reactions. Most notably, electrowetting-on-dielectric (EWOD),^{28,29} electro-dewetting^{15,30} or opto-electrowetting^{31,32} systems can transport discrete droplets by exploiting interactions between the solution and electrified surfaces. For magnetically actuated droplet manipulation,^{33,34} the tilting angle of microplates or micropillar arrays can be swiftly tuned to create a structural anisotropy near

a droplet to realize the controlled droplet transport. Despite remarkable progress, it is still challenging to achieve versatile and robust droplet manipulation without the need of sophisticated surface texturing,³⁵ electrode patterning²⁹ and magnetic structuring.¹⁹ Moreover, the acoustically²⁵ or thermally^{36,37} activated droplet transport usually requires a high energy input.

In recent years, there is a sprout in research using phase change materials, such as paraffin,^{37–43} to lubricate the solid–liquid contact and reversibly modulate droplet mobility. In an early effort to achieve controllable wettability switching, melted paraffin,³⁷ owing to its availability, transparency, chemical stability and biocompatibility, is infused into the porous surface structures to replace the traditional solid–liquid interface with a slippery liquid–liquid interface to facilitate droplet transport. At room temperature, paraffin solidifies and droplets are immobilized due to the strong interaction between water and paraffin molecules. In particular, the programmable transport of droplets with easy integration, minimal energy requirement, and exceptional stability⁴³ has been developed by leveraging the reversible freeze–melt phase transition cycles of paraffin. However, the driving force for droplet transport in relevant methods still comes from external factors, such as earth gravity,^{38,40} and such droplet manipulation strategy hence becomes invalid in microgravity environment or in situations requiring anti-gravity droplet transport.

^aState Key Laboratory of High-performance Precision Manufacturing, Dalian University of Technology, Dalian 116024, China. E-mail: leizhao@dlut.edu.cn

^bKey Laboratory of Icing and Anti/De-icing, China Aerodynamics Research and Development Center, Mianyang, Sichuan 621000, China

† Electronic supplementary information (ESI) available. See DOI: <https://doi.org/10.1039/d3ra01108a>



Herein, we developed an electrothermal platform, *i.e.*, wedge-shaped slippery lubricant-infused porous surface (WS-SLIPS), to realize the spontaneous and controllable droplet transport. The WS-SLIPS features a laser-cut planar wedge structure that creates a substrate curvature gradient to drive the spontaneous droplet transport. The infused paraffin enables WS-SLIPS to rapidly transition from a sticky solid state to a lubricating liquid state to control the droplet transport. We demonstrate that the droplet moving, braking and locking in a programmable manner can be achieved on WS-SLIPS *via* preset electrothermal signals. Besides, WS-SLIPS possesses the broadband liquid-manipulating capability and self-healing feature due to the excellent chemical resistance and interfacial stability, and hence inspires promising applications in microfluidic reactors, bioanalysis, and laboratory-on-a-chip settings.

2. Experimental section

2.1 Fabrication and characterization of WS-SLIPS

The WS-SLIPS integrates the inspirations from both the curvature-gradient feature of cactus spine and the slippery waxy surface of pitcher plant. Fig. 1a illustrates the preparation process of WS-SLIPS. Specifically, an aluminum plate (model 1060, purity 99.6%) was machined into a wedge by a laser cutting system (Han's Laser Technology Industry Group Co.) with a power of 2000 W and scanning speed of 200 mm s^{-1} . The tip width (L_w) and total length (L_0) of the wedge are 2 mm and 80 mm, respectively, while the apex angle (α) varies from 2° to 10° with a step size of 2° . After laser cutting, the substrates were polished with 800# and 1200# sandpapers, followed by rinsing with deionized water and anhydrous ethanol for 2 min, respectively. Microscale textures were produced on the substrate *via* electrochemical etching in a 0.2 mol L^{-1} NaCl (Tianjin Damao Chemical Reagent Factory) solution at a current density of 500 mA cm^{-2} for 10 min. After being thoroughly rinsed with deionized water (resistivity $\sim 18 \text{ M}\Omega$, 1 mPa s ,

Summer-S2-20H, Sichuan Delishi Technology Co., Ltd, China) and dried with nitrogen, they were further placed in a 0.3 mol L^{-1} $\text{H}_2\text{C}_2\text{O}_4$ (Tianjin Damao Chemical Reagent Factory) solution and oxidized at a voltage of 40 V for 15 min to form nanoscale structures (Fig. S1[†]). Fig. 1a presents the scanning electronic micrograph (SEM, SUPRA 55 SAPPHERE, Germany) of the double-tiered surface roughness, where microscale stairs of $\sim 2 \mu\text{m}$ are covered by dense nanoscale dimples. Energy dispersive spectrometer (EDS, SUPRA 55 SAPPHERE, Germany) results further demonstrate that the double-tier porous structures are mainly composed of Al_2O_3 , which was formed in the electrochemical anodic oxidation process, as shown in Fig. S2a[†]. The surface was rendered superhydrophobic by soaking in 0.05 mol L^{-1} stearic acid-ethanol solution for 30 min and baking at 120°C for 1 h, followed by immersion in a liquid paraffin (brand 48#, purchased from Microcrystalline Wax Industry) reservoir at 75°C for 1 h. In this way, liquid paraffin penetrated into the pores and WS-SLIPSs were eventually formed by removing excess paraffin on the surface with dust-free napkins.

The schematic in Fig. 1b shows the droplet maneuvering process. A water droplet remains immobilized on the WS-SLIPS at room temperature due to the sticky solid state of paraffin. A ceramic heating plate with a dimension $90 \text{ mm} \times 15 \text{ mm} \times 1.3 \text{ mm}$ ($1.3\text{--}1.5 \Omega$, 24 V, Guangzhou Baile New Material Co.) is attached to the bottom of WS-SLIPS to exert a uniform Joule heating to the substrate. After the DC power (ZY-500W, 0–60 V, ZhaoYuan Electric) was switched on, paraffin gradually transformed from the sticky solid state to a slippery molten state after reaching the melting temperature $T_m = 50^\circ\text{C}$. In such a case, the unbalanced Laplace pressure introduced by the curvature of wedge-shaped substrate overcomes the surface friction to initiate the spontaneous droplet sliding. Notably, the liquid paraffin solidified quickly and locked the droplet in place as soon as the Joule heating was switched off (Fig. S3[†]). Moreover, the droplet's "moving-locking" cycle can be regulated precisely in the form of not only the transport velocity but also the moving distance.

The contact and sliding angles of the droplets were measured using an OCA25 standard contact angle goniometer (Dataphysics GmbH, Germany). The values of contact and sliding angles were obtained by averaging at least five measurements. The temperature of the ceramic heating pad and WS-SLIPS was measured by a thermal infrared camera (Fotric 288, China). Droplet behavior modulation experiments on the WS-SLIPS surface were recorded by a digital single lens reflex camera (Canon, EOS 80D, Japan).

3. Results and discussion

3.1 Electrothermally switchable wettability of WS-SLIPS

To demonstrate the excellent electrothermal response for rapid and reversible transition between the solid state and the slippery state, we first investigate the temperature variation of WS-SLIPS under different electrothermal conditions using an infrared thermography. As shown in Fig. S4 and Movie S1,[†] the infused paraffin layer on WS-SLIPS is in the solid state at room

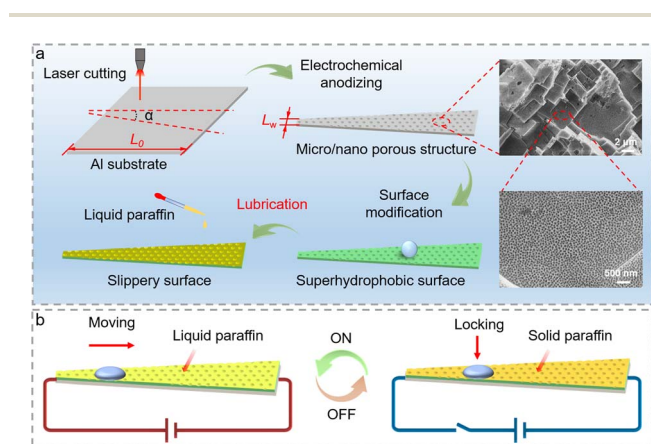


Fig. 1 Fabrication and characterization of the WS-SLIPS. (a) Schematics showing the preparation process of the WS-SLIPS using a hybrid bionic strategy. (b) Schematics showing the control of droplet transport by Joule heating.

temperature, and after turning on the switch, the surface temperature T_s increases and plateaus at a steady value of 43.6 °C, 53.7 °C, 62.2 °C, and 73.4 °C after 200 s Joule heating at $U_0 = 10$ V, 12 V, 14 V, 16 V, respectively (Fig. 2a). Therefore, a voltage larger than 12 V is applied in the later experiment in order to melt the paraffin. After the switch is turned off, the surface temperature drops quickly down below the melting temperature. In this process, micro-cracks gradually develop and propagate as the volume of paraffin layer shrinks substantially during solidification (Fig. S2b†), which act to maximize the pinning effect and immobilize the liquid droplet thereon. The rate of temperature rise and decrease was described by two constants τ_1 and τ_2 , defined as the time required for T_s reaches T_m during the heating process and *vice versa*. Fig. 2b reveals that τ_1 decreases and τ_2 increases as U_0 increases. Obviously, a higher voltage is preferred to improve the response rate of WS-SLIPS transitioning into the lubricating state, while it takes longer to immobilize a sliding droplet on WS-SLIPS after the voltage is turned off. Therefore, the applied voltage should be deliberately selected to leverage the transitioning behaviors of WS-SLIPS to realize the active control of droplet transport.

To investigate the wettability change of WS-SLIPS under the thermal stimulus, we measure the contact angle θ_c and sliding angle θ_s of water droplets on WS-SLIPS. As shown in Fig. 2c, the superhydrophobic surface before infusing paraffin, *i.e.*, SHS, has a contact angle of $\theta_c = 161^\circ$ and a sliding angle of $\theta_s = 3^\circ$, while they are 110° and 85° , respectively, on the solid-state WS-SLIPS, indicating its hydrophobicity but with an extraordinary contact angle hysteresis. This is possibly due to the strong intermolecular interactions between water and paraffin molecules, as well as the microscale surface imperfections developed

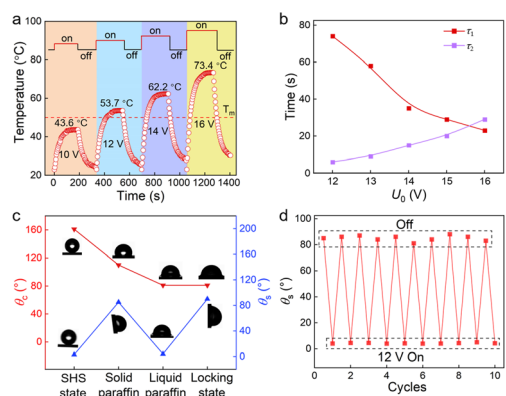


Fig. 2 Switchable wettability of Joule-heated WS-SLIPS. (a) Temperature–time curves of WS-SLIPS under different applied voltages, room temperature $RT = 23$ °C, room humidity $RH = 30\%$. (b) The heating and cooling time of the WS-SLIPS under different applied voltages, each data point is the average of three measurements. (c) Contact angle θ_c and sliding angle θ_s of droplets on different substrates. SHS is the superhydrophobic surface before infusing lubricant. Solid paraffin and liquid paraffin represent the unheated WS-SLIPS and WS-SLIPS heated above T_m , respectively. Locking state indicates the heated WS-SLIPS cools down to the room temperature and the water droplet is enveloped by a thin layer of paraffin. (d) Sliding angle of WS-SLIPS under multiple heating cycles.

during the solidification process. As a result, a water droplet tends to be immobilized once deposited onto the sticky substrate. As WS-SLIPS is heated above the melting temperature, the WS-SLIPS enters the slippery state with $\theta_c = 81^\circ$ and $\theta_s = 4^\circ$. The water droplet now is lubricated by a thin layer of liquid paraffin and is able to spontaneously move along the substrate driving by the Laplace pressure gradient.

Another observation on the WS-SLIPS is the locking of water droplets, which is associated with a solid paraffin layer enveloping the droplet after a heating–cooling cycle. In this work, the surface tension of water droplet, liquid paraffin, and the interfacial tension between water and liquid paraffin are $\gamma = 72.1$ mN m^{-1} , $\gamma_p = 20.0$ mN m^{-1} , and $\gamma_{wp} = 50.3$ mN m^{-1} , respectively. Since $\gamma > \gamma_p + \gamma_{wp}$,⁴⁴ the lubricant spontaneously spread over and cloak the droplet to minimize the total surface energy. The cloaking effect when WS-SLIPS is being heated is further confirmed by our experiments (Fig. S5 and S6, Movie S2†). When the Joule heating is unloaded, the cloaking lubricant solidifies, and after the complete cooldown of WS-SLIPS, the droplet is eventually enveloped by a thin solid paraffin film, which hurdles any droplet motion. We refer to this state as the locking state of WS-SLIPS, because the pinning force is strong enough to lock the droplet in place even when the surface is upside down, *i.e.*, $\theta_s = 180^\circ$ (Fig. S7†). Fig. 2d shows that WS-SLIPS is able to resume the slippery state after being heated again and such a reversible switch of surface wettability can be repeated for 10 cycles of heating and cooling.

3.2 Electrothermally controlled droplet transport on WS-SLIPS

The electrothermally controlled wettability switch of the WS-SLIPS provides a facile way to manipulate the droplet transport. Fig. 3a shows the transport of a 15 μ L on the WS-SLIPS with $\alpha = 6^\circ$, on which the droplet manipulation could be divided into four consecutive stages including moving, braking, locking, and relaunching. Specifically, the WS-SLIPS is first heated at $U_0 = 12$ V and entered into the slippery state (left

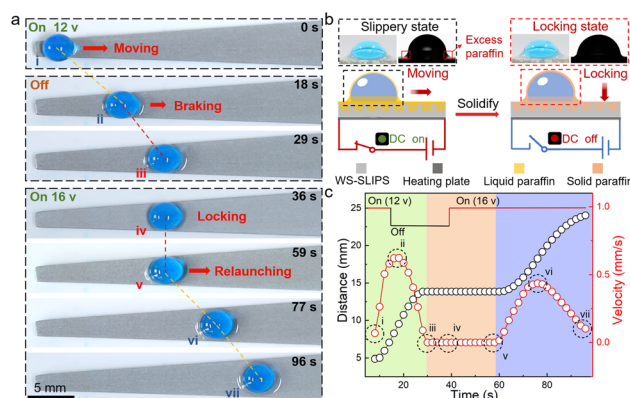


Fig. 3 Electrothermally controlled droplet transport on the WS-SLIPS. (a) Time-lapse images of droplet manipulation on the WS-SLIPS with $\alpha = 6^\circ$. (b) Schematic showing the droplet moving and locking on the WS-SLIPS. (c) Evolution of displacement and velocity of the water droplet.

column in Fig. 3b). The droplet deposited on the surface moves and accelerates with a transport velocity up to 0.7 mm s^{-1} (Circle ii in Fig. 3c) due to the lubrication of liquid paraffin and unbalanced Laplace pressure gradient. After the Joule heating is turned off at $t = 18 \text{ s}$, both the droplet and paraffin begin to cool down and the lubricant starts to transition back to the sticky solid state, under which the lubricant that cloaks the droplet solidifies first, since the droplet temperature is always lower than that of the substrate. During this process, the droplet brakes with its velocity gradually decreasing to 0 (Circle iii in Fig. 3c). At $t = 29 \text{ s}$, the droplet comes into a complete stop and enters the locking state, presented by an enveloping layer of solid paraffin (right column in Fig. 3b). To resume the translational motion of the droplet, we deliberately heat the surface again at $U_0 = 16 \text{ V}$ for a quick relaunching in 23 s (Circle v in Fig. 3c). Notably, the droplet slows down at $t = 77 \text{ s}$ as it becomes unconstrained by the substrate curvature and completely stops at $t = 96 \text{ s}$ with a total travel distance of $\sim 25 \text{ mm}$. Here we argue that more sophisticated manipulation of droplet transport *via* controlling the droplet moving, braking, locking, and relaunching can be realized by leveraging programmed electrothermal signals (Fig. S8†), WS-SLIPS geometry and droplet volume.

3.3 Spontaneous droplet transport on WS-SLIPS

To explain the spontaneous droplet transport on the WS-SLIPS, detailed force analysis is conducted. As shown in Fig. 4a, when a water droplet is deposited onto the tip end of a heated WS-SLIPS with $T_s = 53.7 \text{ }^\circ\text{C}$, it conforms to the wedge shape with unequal radii of curvature at the tip end and tail end. This geometric asymmetry leads to an unbalanced Laplace pressure inside the droplet scaled as

$$P_1 \sim \gamma \frac{1}{r}, \quad P_2 \sim \gamma \frac{1}{R}, \quad (1)$$

where r and R are the local radii of curvature at the tip end and tail end, respectively. Then the driving force F_L can be approximated as^{45–48}

$$F_L \sim \gamma \left(\frac{1}{r} - \frac{1}{R} \right) \frac{\sin 2\alpha}{R-r} V = \frac{\gamma V \sin 2\alpha}{Rr}. \quad (2)$$

Obviously, F_L is proportional to α , which indicates that a larger apex angle facilitates the droplet motion at the early stage. However, F_L gradually decreases as R and r increase during the droplet motion.

Since the contact angle hysteresis is negligible on the slippery WS-SLIPS, the resistance for droplet motion mainly comes from the viscous drag^{49,50} F_H as

$$F_H \sim (\mu_0 + \mu_1)v\pi R \quad (3)$$

where $\mu_0 = 10 \text{ mPa s}$, $\mu_1 = 0.5 \text{ mPa s}$ and v are the lubricant viscosity at $53 \text{ }^\circ\text{C}$, the water viscosity at $50 \text{ }^\circ\text{C}$, and the droplet velocity, respectively. Fig. 4b presents the velocity profile of a moving water droplet of $\sim 20 \mu\text{L}$ on slippery WS-SLIPS. For $\alpha = 10^\circ$, the maximum velocity is $v_{\text{max}} = 2.48 \text{ mm s}^{-1}$, rendering

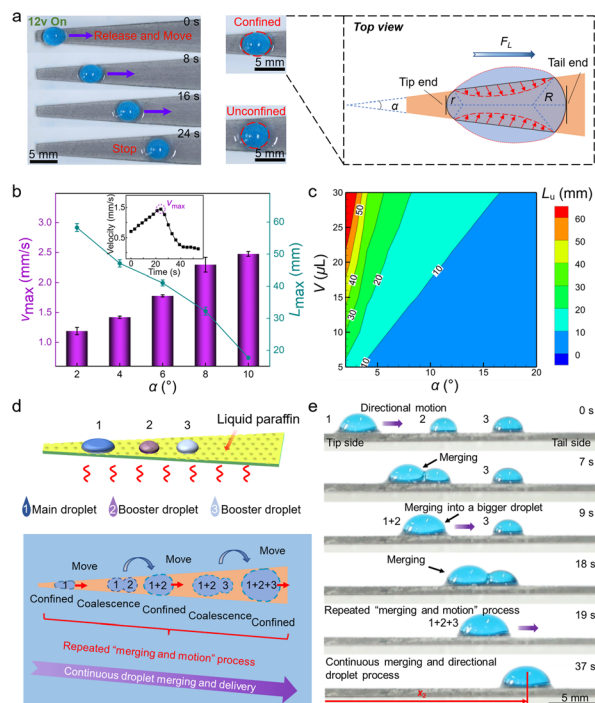


Fig. 4 Mechanism of spontaneous droplet transport on the WS-SLIPS. (a) Optical images of a droplet $\sim 15 \mu\text{L}$ moving on a WS-SLIPS with $\alpha = 8^\circ$. The right side shows the schematic of force analysis. (b) Maximum transport velocity v_{max} and transport distance L_{max} of a water droplet of $\sim 20 \mu\text{L}$ on the WS-SLIPS. The error bars denote standard deviations, obtained from repeated experimental measurements. The inset shows the temporal profile of droplet velocity on the WS-SLIPS with $\alpha = 4^\circ$. (c) Contour plot of L_u at different apex angles α and droplet volume V . (d) Schematic illustration of the droplet fueling strategy on the WS-SLIPS. (e) Time-lapse images of swift and long-distance transport of droplets using the droplet fueling strategy.

a maximum drag $F_H \sim 1.6 \times 10^{-7} \text{ N}$. If we use $R_0 = (4V/3\pi)^{1/3}$ to approximate \sqrt{Rr} in eqn (2), the average driving force is $F_L \sim 2.0 \times 10^{-5} \text{ N}$, which is two orders of magnitude higher than F_H . Therefore, we conclude that the droplet velocity is actually dominated by F_L , which is in turn determined by the apex angle α . In this sense, a higher apex angle is desirable to realize a rapid droplet transport.

The transport distance of water droplets on WS-SLIPS is also affected by α . From eqn (1) and (2), F_L eventually drops to 0 when R equals to r . Therefore, we use L_u where the droplet becomes unconstrained by the substrate curvature to characterize the droplet travel distance

$$L_u = \frac{\left[\frac{3V \sin^3 \theta_c}{\pi(2 + \cos \theta_c)(1 - \cos \theta_c)^2} \right]^{1/3}}{\sin \frac{\alpha}{2}} - \frac{L_w}{2 \tan \frac{\alpha}{2}} \quad (4)$$

where $L_w = 2 \text{ mm}$ is the width of the tip end. Fig. 4c displays the dependence of L_u on α and V , where the droplet travel distance is monotonically decreasing with respect to α , indicating an inherent tradeoff between the droplet velocity and transport distance. Therefore, the apex angle of WS-SLIPS ought to be deliberately designed to achieve swift and long-distance droplet

transport. Fig. 4c also demonstrates that the droplet travel distance can be enhanced by increasing the droplet volume. In this regard, we devise a droplet fueling strategy to increase the droplet travel distance without sacrificing the droplet transport velocity. As shown in Fig. 4d and e, we placed two booster droplets 2 and 3 that are 6.8 mm apart in addition to a main droplet of $\sim 15 \mu\text{L}$ at the tip on slippery WS-SLIPS (Movie S3†). The main droplet firstly moves from the tip and then meets with the first booster droplet 2 to merge into a large droplet 1 + 2. The increased volume of the merged droplet 1 + 2 induces an increased Laplace pressure gradient to sustain the rapid droplet transport until it meets the second booster droplet 3. We mark that using the droplet fueling strategy can transport the droplet for $L_{\text{max}} = 48 \text{ mm}$, a 37% increase compared to single droplet transport (Fig. S9†).

3.4 Versatility of the WS-SLIPS

To further validate the universal applicability of the WS-SLIPS, systematic experiments were conducted on surface of different configurations with different liquids. Fig. 5a shows that a water droplet can climb an inclined substrate against gravity with an average velocity of 0.45 mm s^{-1} . Moreover, droplet merging chemical reactions are available on WS-SLIPS. Fig. 5b shows an experiment of controlled colored reaction between starch solution and iodine solution. The white starch drops is transported by the WS-SLIPS and then merge with an iodine solution

drop to complete the colored reaction in 30 s. In addition, multiple droplets can be controlled simultaneously or sequentially by the time-sharing control of the WS-SLIPS to complete multi-step reactions. For example, separate droplets on the WS-SLIPS in a symmetric configuration converge to the joint simultaneously with identical velocities, as shown in Fig. 5c and d. Also, the sequence of droplet coalescence can be controlled on-demand by adjusting the electrical voltage applied on each branch (Fig. 5e), which gives rise to exciting applications in micro-sampling, microanalysis where multiple reagents need to meet and mix with specific sequence to complete chemical reactions. Fig. 5f further shows the delicate control of droplet speeding up, turning, stop, and restarting on a spiral-shaped WS-SLIPS (Movie S4†).

The slippery property of the WS-SLIPS offers the intrinsic advantage that the surface scratches can be automatically self-healed using Joule heating to melt and flatten the surface (Fig. S10 and Movie S5†). As shown in Fig. 5g, the WS-SLIPS were scratched by a knife at room temperature, resulting in several visible trenches on the sample. Although seriously damaged, we show that the droplet manipulation capability of WS-SLIPS is unaffected. A water droplet is placed at the tip end of damaged WS-SLIPS as shown in Fig. 5g. When WS-SLIPS is connected to $U_0 = 16 \text{ V}$, the surface trenches are gradually being filled once the surface temperature rises above its melting temperature. In the meantime, the droplet starts to move along the sample and

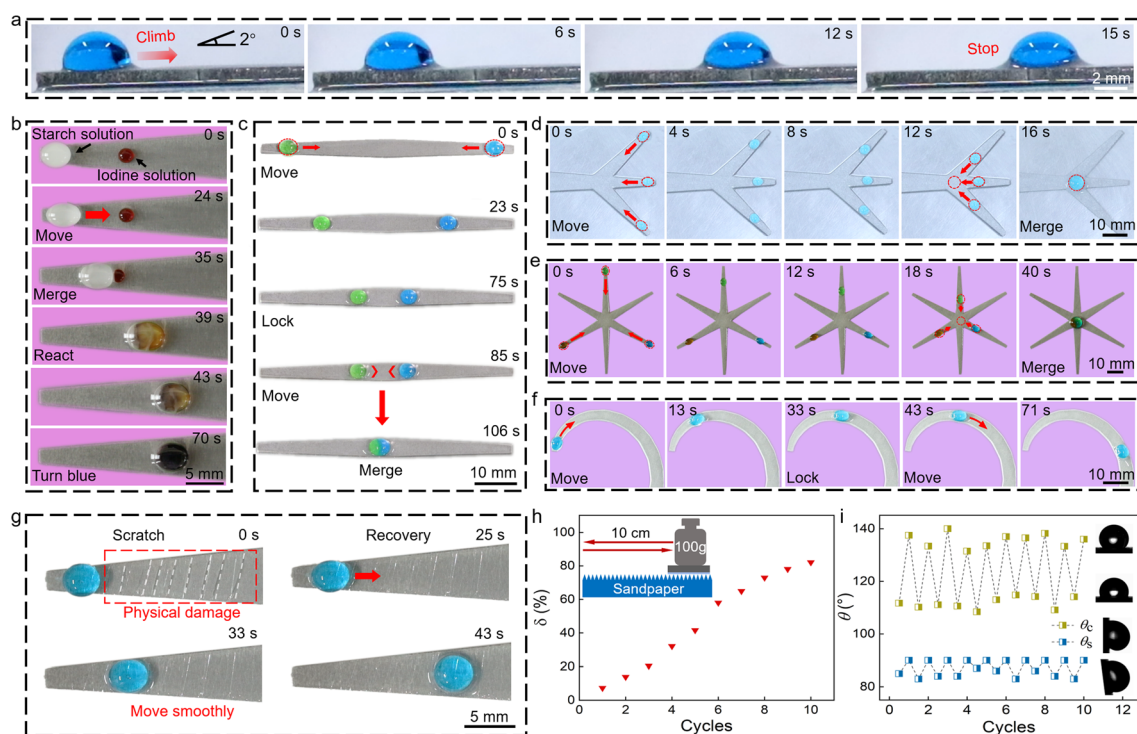


Fig. 5 Application of WS-SLIPS in droplet manipulation. (a) Optical image of a $20 \mu\text{L}$ droplet moving against gravity on WS-SLIPS with $\alpha = 8^\circ$ and an inclination angle of 2° . (b) Chemical colour reaction of starch solution droplet with iodine solution droplet on a single WS-SLIPS. (c) Controlled droplet transport and coalescence on a compass-shaped WS-SLIPS. (d) Controlled merging of three separate droplets on a tree-like WS-SLIPS. (e) Controlled droplet merging on a hexagonal WS-SLIPS. (f) Three-dimensional droplet manipulation on a spiral WS-SLIPS. (g) Droplet transport on scratched samples. (h) Mass change of WS-SLIPS during the sandpaper abrasion test. (i) Contact angle and sliding angle of water on WS-SLIPS during the sandpaper abrasion test.

eventually stops at $t = 43$ s with all trenches flattened. The durability of WS-SLIPS against mechanical abrasion is shown in Fig. 5h. WS-SLIPS is put face down on the sandpaper (standard sandpaper, #240) with 100 grams of weights on it. The sample is moved for 10 cm, rotated by 90° and then moved for another 10 cm to make sure the sample is abraded longitudinally and transversely. This process is defined as an abrasion cycle. The sample is heated above its melting temperature after each abrasion cycle before entering the next cycle, during which the sample mass, static contact angle θ_c of water, and sliding angle θ_s of water are recorded as shown in Fig. 5i. It is found that WS-SLIPS can fully restore the liquid-repellency and droplet manipulating capability even after 10 abrasion cycles, the paraffin acts like a protective shell to protect the microscale surface structures of WS-SLIPS from being damaged in each abrasion cycle. In addition, we also conducted droplet manipulation experiment under low temperature environment. When the temperature is 0°C , WS-SLIPS can still complete droplet manipulation under $U_0 = 16$ V, which provides a feasible strategy for droplet manipulation under cold environments (Fig. S11†).

The WS-SLIPS can be harnessed as an electrothermal platform to actively manipulate not only water, but also organic/inorganic solutions with varying surface tension and viscosity. We use saturated NaCl solution, ethanol solution (volume fraction of 10%) and glycerol to showcase the broadband manipulation capability of WS-SLIPS, since those three solutions are most common liquids being used in daily life and laboratory applications. It is found that on the sticky solid-state WS-SLIPS, a strong contact angle hysteresis with the sliding angle around $\theta_s = 80^\circ$ exists for all three liquids. When the WS-SLIPS is heated into the slippery state, θ_s decreases drastically to around 3° , demonstrating the excellent lubricating effect of liquid paraffin (Fig. 6a–c) on different liquids. Note that the locking state of WS-SLIPS after a heating–cooling cycle is also

present for all three liquids, suggesting that it is a universal feature of WS-SLIPS. Fig. 6d–f shows that the moving, braking, locking and relaunching of all liquid droplets can be realized by utilizing the sticky, slippery and locking states of WS-SLIPS. We also made a series of ethanol/water solutions with the volume fraction of ethanol varying from 0% to 50%. As the surface tension of the ethanol/water solution decreases down to 28.1 mN m^{-1} , the droplet moving velocity remains unchanged, further demonstrating the versatility of WS-SLIPS (Fig. S12†).

4. Conclusion

In summary, we propose WS-SLIPS as a versatile and robust platform to manipulate the moving, braking, locking and relaunching of liquid droplets by electrothermal actions. The driving force for droplet transport originates from the unbalanced Laplace pressure induced by the curvature gradient of the wedge-shaped substrate. Infusing the wedge-shaped substrate with phase-changeable paraffin endows the surface with the ability to conveniently switch the wettability between a sticky solid-state, a slippery lubricating state and a unique locking state under proper electrical signals. We demonstrate that the on-demand liquid manipulation on WS-SLIPS can be realized *via* preset electrical signals. The force analysis on the droplet dynamics on WS-SLIPS reveals that both the droplet velocity and travel distance can be controlled by adjusting the electrical voltage, the apex angle and the droplet volume. In addition, WS-SLIPS can be used in manipulating different organic/inorganic droplets, including saturated NaCl solution, ethanol solution and glycerol. The self-healing feature also enables the WS-SLIPS to automatically repair itself from mechanical scratches and warrants extensive applications in more diverse situations. The removing, mixing, reacting and separating of single micro-volume droplet as well as the intelligent regulation in the droplet transport channel can finally realize the collection, transportation, storage and manipulation of droplet, which promises important applications in digital microfluidics, chip cooling and biomedical sampling.

Author contributions

The manuscript was written through contributions of all authors. All authors have given approval to the final version of the manuscript.

Conflicts of interest

The authors declare no competing financial interest.

Acknowledgements

This work was supported by the National Key Research and Development Program of China (2022YFB4602401), National Natural Science Foundation of China (52075071, 52105174), Opening Project of the Key Laboratory of Bionic Engineering (Ministry of Education), Jilin University (KF20200002), and Key

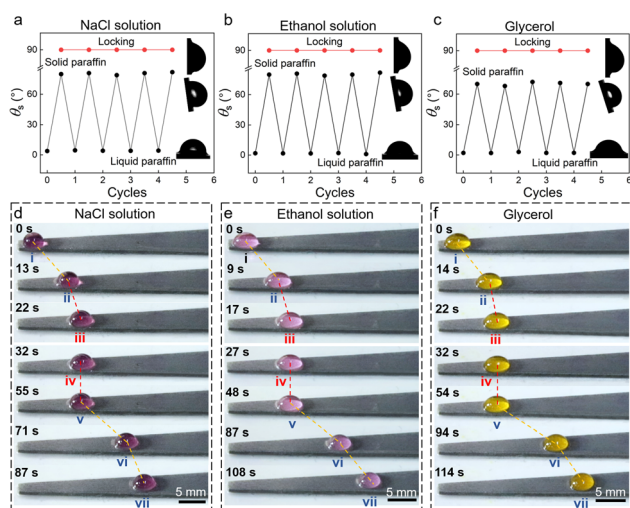


Fig. 6 Manipulation of various liquids on WS-SLIPS. The sliding angle θ_s of (a) saturated NaCl solution, (b) ethanol solution (volume fraction of 10%, $\sim 5\ \mu\text{L}$) and (c) glycerol. Time-lapsed images of droplet ($\sim 10\ \mu\text{L}$) manipulation of (d) NaCl solution, (e) ethanol solution (volume fraction of 10%) and (f) glycerol on WS-SLIPS, scale bar: 5 mm.

Laboratory of Icing and Anti/De-icing of CARDC (Grant No. IADL 20210405).

Notes and references

- 1 J. Seo, S. Lee, J. Lee, J. Seung Lee, H. Kwon, S. Cho, J. Ahn and T. Lee, *Sci. Rep.*, 2015, **5**, 12326.
- 2 H. Hiram, S. Yoshii, Y. Komazaki, S. Kano, T. Torii and H. Mekaru, *Chem. Lett.*, 2021, **50**, 213–216.
- 3 Y. Zhang and T. Wang, *Adv. Mater.*, 2013, **25**, 2903–2908.
- 4 E. Samiei, M. Tabrizian and M. Hoorfar, *Lab Chip*, 2016, **16**, 2376–2396.
- 5 G. Huang, M. Li, Q. Yang, Y. Li, H. Liu, H. Yang and F. Xu, *ACS Appl. Mater. Interfaces*, 2017, **9**, 1155–1166.
- 6 E. Ueda, F. L. Geyer, V. Nedashkivska and P. A. Levkin, *Lab Chip*, 2012, **12**, 5218–5224.
- 7 L. Xu, Y. Chen, G. Yang, W. Shi, B. Dai, G. Li, Y. Cao, Y. Wen, X. Zhang and S. Wang, *Adv. Mater.*, 2015, **27**, 6878–6884.
- 8 A. A. Popova, K. Demir, T. G. Hartanto, E. Schmitt and P. A. Levkin, *RSC Adv.*, 2016, **6**, 38263–38276.
- 9 X. Dai, N. Sun, S. O. Nielsen, B. B. Stogin, J. Wang, S. Yang and T. S. Wong, *Sci. Adv.*, 2018, **4**, q919.
- 10 Z. Peng, Y. Chen and T. Wu, *ACS Appl. Mater. Interfaces*, 2020, **12**, 47299–47308.
- 11 Z. Cui, L. Xiao, Y. Li, Y. Zhang, G. Li, H. Bai, X. Tang, M. Zhou, J. Fang, L. Guo, S. Liu, C. Xiao and M. Cao, *J. Mater. Chem. A*, 2021, **9**, 9719–9728.
- 12 X. Liang, V. Kumar, F. Ahmadi and Y. Zhu, *Droplet*, 2022, **1**, 80–91.
- 13 L. Zhang, Z. Guo, J. Sarma, W. Zhao and X. Dai, *Adv. Funct. Mater.*, 2021, **31**, 2008614.
- 14 X. Leng, L. Sun, Y. Long and Y. Lu, *Droplet*, 2022, **1**, 139–169.
- 15 P. Che, L. Heng and L. Jiang, *Adv. Funct. Mater.*, 2017, **27**, 1606199.
- 16 Z. Wang, L. Heng and L. Jiang, *J. Mater. Chem. A*, 2018, **6**, 3414–3421.
- 17 H. Dai, C. Gao, J. Sun, C. Li, N. Li, L. Wu, Z. Dong and L. Jiang, *Adv. Mater.*, 2019, **31**, 1905449.
- 18 J. Li, N. S. Ha, T. L. Liu, R. M. van Dam and C. C. Kim, *Nature*, 2019, **572**, 507–510.
- 19 J. Guo, D. Wang, Q. Sun, L. Li, H. Zhao, D. Wang, J. Cui, L. Chen and X. Deng, *Adv. Mater. Interfaces*, 2019, **9**, 1900653.
- 20 P. Guo, Z. Wang, L. Heng, Y. Zhang, X. Wang and L. Jiang, *Adv. Funct. Mater.*, 2019, **29**, 1808717.
- 21 C. Son, B. Ji, J. Park, J. Feng and S. Kim, *Micromachines*, 2021, **12**, 325.
- 22 B. L. Wang, L. Heng and L. Jiang, *ACS Appl. Mater. Interfaces*, 2018, **10**, 7442–7450.
- 23 J. Wang, Y. Huang, K. You, X. Yang, Y. Song, H. Zhu, F. Xia and L. Jiang, *ACS Appl. Mater. Interfaces*, 2019, **11**, 7591–7599.
- 24 H. Zhan, Y. Xia, Y. Liu, H. Sun, W. Ge, S. Feng and Y. Liu, *Adv. Funct. Mater.*, 2023, **33**, 2211317.
- 25 D. Foresti, M. Nabavi, M. Klingauf, A. Ferrari and D. Poulidakos, *Proc. Natl. Acad. Sci.*, 2013, **110**, 12549–12554.
- 26 K. Hasegawa, A. Watanabe and Y. Abe, *Sci. Rep.*, 2019, **9**, 16603.
- 27 M. H. Biroun, M. Rahmati, R. Tao, H. Torun, M. Jangi and Y. Fu, *Langmuir*, 2020, **36**, 10175–10186.
- 28 X. Xu, Y. Zhang and L. Sun, *Chin. J. Phys.*, 2018, **56**, 2887–2896.
- 29 J. Cao, Q. An, Z. Liu, M. Jin, Z. Yan, W. Lin, L. Chen, P. Li, X. Wang, G. Zhou and L. Shui, *Sens. Actuators, B*, 2019, **291**, 470–477.
- 30 X. He, J. Zhang, X. Zhang and Y. Deng, *Soft Matter*, 2019, **15**, 5211–5219.
- 31 S. N. Pei, J. K. Valley, Y. Wang and M. C. Wu, *J. Lightwave Technol.*, 2015, **33**, 3486–3493.
- 32 E. Liu, C. Wang, H. Zheng, S. Song, A. Riaud and J. Zhou, *Sens. Actuators, B*, 2022, **368**, 132231.
- 33 S. Ben, T. Zhou, H. Ma, J. Yao, Y. Ning, D. Tian, K. Liu and L. Jiang, *Adv. Sci.*, 2019, **6**, 1900834.
- 34 Y. Fang, J. Liang, X. Bai, J. Yong, J. Huo, Q. Yang, X. Hou and F. Chen, *Langmuir*, 2020, **36**, 15403–15409.
- 35 K. C. Park, P. Kim, A. Grinthal, N. He, D. Fox, J. C. Weaver and J. Aizenberg, *Nature*, 2016, **531**, 78–82.
- 36 S. Wu, L. Zhou, C. Chen, L. Shi, S. Zhu, C. Zhang, D. Meng, Z. Huang, J. Li, Y. Hu and D. Wu, *Langmuir*, 2019, **35**, 13915–13922.
- 37 X. Yao, J. Ju, S. Yang, J. Wang and L. Jiang, *Adv. Mater.*, 2014, **26**, 1895–1900.
- 38 C. Chen, Z. Huang, Y. Jiao, L. Shi, Y. Zhang, J. Li, C. Li, X. Lv, S. Wu, Y. Hu, W. Zhu, D. Wu, J. Chu and L. Jiang, *ACS Nano*, 2019, **13**, 5742–5752.
- 39 C. Chen, L. Zhou, L. Shi, S. Zhu, Z. Huang, C. Xue, J. Li, Y. Hu, D. Wu and J. Chu, *ACS Appl. Mater. Interfaces*, 2020, **12**, 1895–1904.
- 40 W. Gao, J. Wang, X. Zhang, L. Sun, Y. Chen and Y. Zhao, *Chem. Eng. J.*, 2020, **381**, 122612.
- 41 K. Manabe, T. Matsubayashi, M. Tenjimabayashi, T. Moriya, Y. Tsuge, K. Kyung and S. Shiratori, *ACS Nano*, 2016, **10**, 9387–9396.
- 42 K. Okada, Y. Miura, T. Chiya, Y. Tokudome and M. Takahashi, *RSC Adv.*, 2020, **10**, 28032–28036.
- 43 J. Wang, W. Gao, H. Zhang, M. Zou, Y. Chen and Y. Zhao, *Sci. Adv.*, 2018, **4**, t7392.
- 44 D. J. Preston, Y. Song, Z. Lu, D. S. Antao and E. N. Wang, *ACS Appl. Mater. Interfaces*, 2017, **9**, 42383–42392.
- 45 K. Li, J. Ju, Z. Xue, J. Ma, L. Feng, S. Gao and L. Jiang, *Nat. Commun.*, 2013, **4**, 2276.
- 46 C. Zhang, B. Zhang, H. Ma, Z. Li, X. Xiao, Y. Zhang, X. Cui, C. Yu, M. Cao and L. Jiang, *ACS Nano*, 2018, **12**, 2048–2055.
- 47 Y. Chen, K. Li, S. Zhang, L. Qin, S. Deng, L. Ge, L. Xu, L. Ma, S. Wang and X. Zhang, *ACS Nano*, 2020, **14**, 4654–4661.
- 48 L. Xiao, G. Li, Y. Cai, Z. Cui, J. Fang, H. Cheng, Y. Zhang, T. Duan, H. Zang, H. Liu, S. Li, Z. Ni and Y. Hu, *Chem. Eng. J.*, 2020, **399**, 125139.
- 49 B. Nada, G. Henri-Louis, B. S. Srinivas, K. Hyuk-Min, Q. David and K. V. Kripa, *Phys. Rev. Fluids*, 2016, **1**, 063902.
- 50 H. Hwang, P. Papadopoulos, S. Fujii and S. Wooh, *Adv. Funct. Mater.*, 2022, **32**, 2111311.